



Irwin, P. G. J., Toledo, D., Garland, R., Teanby, N. A., Fletcher, L. N., Orton, G. A., & Bézard, B. (2018). Detection of hydrogen sulfide above the clouds in Uranus's atmosphere. *Nature Astronomy*, 2(5), 420-427. <https://doi.org/10.1038/s41550-018-0432-1>

Peer reviewed version

Link to published version (if available):  
[10.1038/s41550-018-0432-1](https://doi.org/10.1038/s41550-018-0432-1)

[Link to publication record in Explore Bristol Research](#)  
PDF-document

This is the author accepted manuscript (AAM). The final published version (version of record) is available online via Nature at <https://www.nature.com/articles/s41550-018-0432-1> . Please refer to any applicable terms of use of the publisher.

## University of Bristol - Explore Bristol Research

### General rights

This document is made available in accordance with publisher policies. Please cite only the published version using the reference above. Full terms of use are available: <http://www.bristol.ac.uk/red/research-policy/pure/user-guides/ebr-terms/>

# 1 **Detection of hydrogen sulphide (H<sub>2</sub>S) above the clouds in** 2 **Uranus' atmosphere**

3 Patrick G. J. Irwin<sup>1</sup>, Daniel Toledo<sup>1</sup>, Ryan Garland<sup>1</sup>, Nicholas A. Teanby<sup>2</sup>, Leigh N. Fletcher<sup>3</sup>,  
4 Glenn A. Orton<sup>4</sup>, & Bruno Bézard<sup>5</sup>

5 <sup>1</sup>*Department of Physics (Atmospheric, Oceanic and Planetary Physics), University of Oxford,*  
6 *Parks Rd, Oxford, OX1 3PU, UK.*

7 <sup>2</sup>*School of Earth Sciences, University of Bristol, Wills Memorial Building, Queens Road, Bristol,*  
8 *BS8 1RJ, UK.*

9 <sup>3</sup>*Department of Physics & Astronomy, University of Leicester, University Road, Leicester,*  
10 *LE1 7RH, UK.*

11 <sup>4</sup>*Jet Propulsion Laboratory, California Institute of Technology, 4800 Oak Grove Drive, Pasadena,*  
12 *CA 91109, USA*

13 <sup>5</sup>*LESIA, Observatoire de Paris, PSL Research University, CNRS, Sorbonne Universités, UPMC*  
14 *Univ. Paris 6, Université Paris-Diderot, Sorbonne Paris Cité, 5 place Jules Janssen, 92195 Meudon,*  
15 *France.*

16 **The main cloud deck on Uranus is observed from visible to near-infrared observations to have**  
17 **a cloud-top pressure of somewhere between 1.2 and 3 bar. However, its composition has never**  
18 **been unambiguously identified, although it is widely assumed to be composed primarily of**  
19 **either ammonia (NH<sub>3</sub>) or hydrogen sulphide (H<sub>2</sub>S) ice. Here we present evidence of a clear**  
20 **detection of gaseous H<sub>2</sub>S above this cloud deck in the wavelength region 1.57 – 1.59 μm**

21 **with a mole fraction of 0.4 – 0.8 ppm at the cloud tops. Its detection constrains the deep**  
22 **bulk sulphur/nitrogen abundance to exceed 4.4 – 5.0 times the solar value in Uranus’ bulk**  
23 **atmosphere, and places a lower limit on the mole fraction of H<sub>2</sub>S below the observed cloud**  
24 **of  $(1.0 – 2.5) \times 10^{-5}$ . The detection of gaseous H<sub>2</sub>S at these pressure levels adds to the weight**  
25 **of evidence that the principal constituent of 1.2 – 3-bar cloud is likely to be H<sub>2</sub>S ice.**

26 In the absence of any spectrally identifiable ice absorption features, the identity of the main  
27 component of the cloud in Uranus’ atmosphere with cloud top pressure 1.2 – 3 bar<sup>1-3</sup> has long  
28 been a source of debate, although authors have most commonly ascribed it to be composed of  
29 either ammonia (NH<sub>3</sub>) or hydrogen sulphide (H<sub>2</sub>S) ice<sup>3</sup>. This is based on the assumed presence  
30 at deeper pressures ( $\sim 40$  bar) of an ammonium hydrosulphide (NH<sub>4</sub>SH) cloud, which combines  
31 together in equal parts any available H<sub>2</sub>S and NH<sub>3</sub>, leaving the remaining more abundant molecule  
32 to condense alone at lower pressures<sup>4</sup>. Deeper in the atmosphere (20 – 40 bar), observations of  
33 Uranus and Neptune at microwave wavelengths (1 – 20 cm) with the Very Large Array (VLA)<sup>5</sup>  
34 found that there was a missing component of continuum absorption, which was concluded to be  
35 likely due to the pressure-broadened wings of H<sub>2</sub>S lines with wavelengths of less than a few mm.  
36 The deep abundance of H<sub>2</sub>S was estimated to be 10 – 30 $\times$  solar and this analysis further concluded,  
37 building upon previous studies<sup>6,7</sup>, that the bulk S/N ratio must exceed  $\sim 5\times$  the assumed solar  
38 ratio<sup>8</sup> in order that the bulk abundance of H<sub>2</sub>S exceeds that of NH<sub>3</sub>, leaving residual H<sub>2</sub>S above  
39 the deeper NH<sub>4</sub>SH cloud. Hydrogen sulphide is believed to be a significant component of all  
40 the giant planet atmospheres and has been detected *in situ* in Jupiter’s deep atmosphere by the  
41 Galileo probe mass spectrometer<sup>9</sup> (and also in comets, both *in situ* and remotely<sup>10,11</sup>). However,

42 it has never been unambiguously remotely detected in the atmospheres of any of the giant planets,  
43 aside from a possible debated detection in Jupiter’s atmosphere following the impact of Comet  
44 Shoemaker-Levy 9 in 1994<sup>12,13</sup>. Hence, while H<sub>2</sub>S is probably the source of the missing continuum  
45 absorption at microwave wavelengths in Uranus and Neptune’s atmospheres, and is also probably  
46 the main component of the 1.2 – 3-bar cloud, it has never been unequivocally detected in Uranus’  
47 atmosphere to confirm this.

48         Detection of H<sub>2</sub>S and NH<sub>3</sub> absorption features at thermal-IR wavelengths is very challenging  
49 due to the extremely cold atmospheric temperatures in Uranus’ atmosphere, but at visible/near-  
50 infrared wavelengths, there are weak absorption bands that could potentially be detected in sun-  
51 light reflected from the cloud tops at wavelengths where the absorption of other gases is weak.  
52 The available line data for the key condensable volatiles in Uranus’ atmosphere (i.e. CH<sub>4</sub>, NH<sub>3</sub>,  
53 H<sub>2</sub>S) have recently been greatly improved and, although these absorptions are weak, we looked to  
54 see whether we could detect these features in near-IR ground-based high resolution spectroscopic  
55 measurements.

56         Observations of Uranus (with adaptive optics) were made with Gemini-North’s Near-infrared  
57 Integral Field Spectrometer (NIFS) instrument in 2009/2010<sup>14,15</sup>. NIFS records 3'' × 3'' image  
58 ‘cubes’ with a pixel size of 0.103 × 0.043'', where each pixel is a spectrum covering, in the H-band,  
59 the wavelength range 1.476 – 1.803 μm with a spectral resolution of R = 5290. For this study we  
60 used observations recorded on 2nd November 2010 at approximately 06:00UT<sup>15</sup>. To minimise  
61 random noise we averaged the observations over seven 5 × 5 pixel boxes, indicated in Fig. 1 and

62 listed in Table 1. We selected the wavelength region  $1.49 - 1.64 \mu\text{m}$  for our analysis, comprising  
63  $n_y = 937$  spectral points. We initially set the noise at each wavelength to be the variance of data  
64 in these  $5 \times 5$  pixel boxes. However, we found that we were not quite able to fit these spectra to  
65 a precision of  $\chi^2/n_y \sim 1$  and attributed this to unknown deficiencies in our spectral modelling.  
66 We thus multiplied these errors by a single factor of 1.6 at all wavelengths (except for area ‘6’, for  
67 which the variance was already sufficiently large) to account for these ‘forward-modelling’ errors.  
68 For our reference spectrum we chose the region close to the disc centre, centred at  $15.3^\circ\text{N}$  (Area  
69 ‘1’), but performed the same analysis for all other selected regions, reported in the supplementary  
70 material.

71 To model the observed spectra we used the NEMESIS<sup>16</sup> retrieval model, using the correlated-  
72 k approximation with ‘k’-tables generated from the recently published WKLMC@80K+<sup>17</sup> line  
73 data for  $\text{CH}_4$  and updated line data for  $\text{H}_2\text{S}$  and  $\text{NH}_3$  from HITRAN2012<sup>18</sup>. The mean absorption  
74 strengths of  $\text{CH}_4$ ,  $\text{NH}_3$  and  $\text{H}_2\text{S}$  across the H-band wavelength range contained in these data (cal-  
75 culated at 100 K and 1 atm) are shown in Fig. 1. Our *a priori* vertical atmospheric profile was  
76 based on the ‘F1’ temperature profile, determined from HST/STIS and Voyager 2 observations<sup>3</sup>.  
77 This profile has a deep methane mole fraction of 4%<sup>19</sup>, and has a varying relative humidity with  
78 height above the condensation level. The He: $\text{H}_2$  ratio was set to 0.131 and the profile includes  
79 0.04% mole fraction of Ne<sup>3</sup>. To this profile we added  $\text{NH}_3$  and  $\text{H}_2\text{S}$ , assuming arbitrary ‘deep’  
80 mole fractions (i.e. above the putative  $\text{NH}_4\text{SH}$  cloud) of 0.1% for both, and limited their abun-  
81 dance to not exceed the saturated vapour pressure<sup>20</sup> in the troposphere as the temperature falls with  
82 height, adjusting the abundance of hydrogen and helium (keeping He: $\text{H}_2$  = 0.131) to ensure the

83 mole fractions summed to unity at each pressure level. Figure 2 shows the modelled abundance  
84 profiles of the three condensible species falling with height. We can see that the saturated vapour  
85 pressure of H<sub>2</sub>S at the pressure of the main clouds of Uranus (1.2 – 3 bar) is approximately 2000  
86 times higher than that of NH<sub>3</sub>. Hence, even though the peak NH<sub>3</sub> absorption strength in this spec-  
87 tral region is, from Fig. 1, ~ 100 times stronger than that of H<sub>2</sub>S, we expect the absorption lines  
88 of H<sub>2</sub>S to be far more visible due to the higher likely abundance of H<sub>2</sub>S and also the lines of H<sub>2</sub>S  
89 having maximum strength at wavelengths of minimum methane opacity (Fig. 1). The very low  
90 saturated vapour pressure of NH<sub>3</sub> at the 1.2–3 bar level in Uranus’ atmosphere makes it likely that  
91 NH<sub>3</sub> would not have enough abundance to condense into a cloud with sufficient opacity at this  
92 level as has previously been noted<sup>3</sup>.

93 We fitted the spectrum using a multiple-scattering model and modelled cloud opacity with  
94 a vertically continuous profile of particles (at 39 levels) with a Gamma size distribution of mean  
95 radius 1.0  $\mu\text{m}$  and variance 0.05. This size distribution is typical of that assumed in previous  
96 analyses<sup>2,21</sup>, but is an assumption and is not constrained by, for example, a microphysical model.  
97 In addition, the assumption that the particles have the same size distribution at all altitudes is  
98 an oversimplification since we would expect that in real clouds the particles would be smaller at  
99 higher altitudes. However, the primary objective of this study was to search for the spectral sig-  
100 nature of H<sub>2</sub>S gas, rather than to fit a sophisticated cloud model and we thus chose a model that  
101 would be simple and easy to fit. It should be noted that our simple cloud model is used to model  
102 not only the effects of the main 1.2 – 3 bar cloud, but also any CH<sub>4</sub> cloud opacity and any tropo-  
103 spheric/stratospheric haze opacity that may be present. In addition to fitting the cloud opacity at

104 each level in the atmosphere, we also fitted the imaginary refractive index spectrum of the parti-  
 105 cles (assumed to be the same at all vertical levels) at nine wavelengths between 1.4 and 1.8  $\mu\text{m}$ ,  
 106 reconstructing the real part of the refractive index spectrum using the Kramers-Kronig relation<sup>21</sup>,  
 107 assuming  $n_{real} = 1.4$  at 1.6  $\mu\text{m}$ . We constrained the imaginary refractive index spectrum to vary  
 108 reasonably slowly with wavelength, to avoid degeneracy with the H<sub>2</sub>S signal we were trying to de-  
 109 tect (see Methods). Self-consistent extinction cross-sections, single-scattering albedos and phase  
 110 functions were then computed at all wavelengths using Mie theory, with the phase functions ap-  
 111 proximated with Henyey-Greenstein functions (see Methods section). The total number of variable  
 112 parameters in our retrieval was thus  $n_x = 39 + 9 = 48$ , and thus the total number of degrees of  
 113 freedom,  $n = n_y - n_x$  was 889.

114 Figure 3 shows our fit to the reference Uranus spectrum (Area ‘1’ of Fig. 1 and Table 1)  
 115 when H<sub>2</sub>S and NH<sub>3</sub> absorption is neglected, using three different *a priori* values of the imaginary  
 116 refractive index of 0.001, 0.01 and 0.1, respectively, at all wavelengths with an *a priori* error  
 117 of  $\pm 50\%$ . We can see that reasonably good fits are achieved for all three cases, but that better  
 118 fits are achieved with higher *a priori* values, with similar results for  $n_i = 0.01$  and  $n_i = 0.1$   
 119 ( $\chi^2/n \sim 1.7$ ). For the  $n_i = 0.001$  case, a poorer fit is achieved ( $\chi^2/n \sim 1.9$ ) as the solution cannot  
 120 move far enough away from the *a priori* to properly fit the spectrum. As a result the retrieved  
 121 particles have low imaginary refractive index and so are more scattering, necessitating the cloud  
 122 profile opacity to reduce quickly at pressures greater than 2–3 bar to prevent significant reflection  
 123 from these levels. This is in stark contrast to the other two solutions, where  $n_i$  is much higher  
 124 ( $n_i \sim 0.06$ ), and where we find that the single-scattering albedo of the particles is  $\varpi = 0.7–0.8$  and

125 phase function asymmetry is  $g \sim 0.7$  across the observed spectral range (Supplementary Fig.1).  
126 These retrieved single-scattering albedo and phase-function asymmetry values agree very well  
127 with a limb-darkening analysis<sup>14</sup>, which used these same Gemini/NIFS data smoothed to a lower  
128 resolution of FWHM = 0.004  $\mu\text{m}$  and older, lower-resolution methane absorption k-distribution  
129 data<sup>22</sup>, and also with an analysis of Keck and HST images<sup>23</sup>, which recommended  $\varpi = 0.75$  and  
130  $g = 0.7$ . An important consequence of the low single-scattering albedo of the retrieved particles is  
131 that solar photons are quickly absorbed as they reach the cloud tops and so we do not see significant  
132 reflection from particles residing at pressures greater than 2–3 bar. This can be seen in the retrieved  
133 error bars for the cloud opacity profiles in Fig. 3 quickly relaxing back to their *a priori* value as  
134 the pressure increases and the profiles for the higher  $n_i$  values tending smoothly back to their *a*  
135 *priori* opacity/bar values. As a result, although we can clearly detect the cloud-top pressure at these  
136 wavelengths, we cannot tell where the base is and thus cannot differentiate between a vertically  
137 thin cloud based at 2–3 bar, or a cloud that extends vertically down to several bars with the same  
138 cloud-top pressure. We also note here that when the particles are constrained to be more scattering,  
139 the peak of cloud opacity is at a lower pressure than for the case with more absorbing particles.  
140 This phenomenon may help to explain why HST/STIS<sup>3</sup> retrievals, which assume the particles to  
141 be more scattering, find the cloud tops to be at lower pressures (1.2 bar) than retrievals near 1.5  
142  $\mu\text{m}$ <sup>1,2</sup>, which assume more absorbing particles and find cloud tops at 2–3-bar.

143 Figure 4 compares our best fits to the observed reference spectrum (Area ‘1’ at 15.3°N) in  
144 the 1.56 – 1.60  $\mu\text{m}$  region, including or excluding H<sub>2</sub>S absorption. When H<sub>2</sub>S absorption is not in-  
145 cluded, we find that there is a significant discrepancy between the measured and modelled spectra,



146 giving  $\chi^2/n = 1.71$ . This discrepancy is significantly reduced when H<sub>2</sub>S absorption is included and  
147 NEMESIS allowed to scale the abundance of H<sub>2</sub>S, achieving a much closer fit with  $\chi^2/n = 1.30$ .  
148 When H<sub>2</sub>S absorption is not included, there are several peaks in the difference spectrum (Fig. 4)  
149 that match perfectly the effect of including or excluding this gas in the spectral calculation. We ex-  
150 amined the correlation between the expected H<sub>2</sub>S signal and this difference spectrum between 1.57  
151 and 1.60  $\mu\text{m}$ , and found a Pearson correlation coefficient of 0.718 (indicating a strong correlation)  
152 and a Spearman rank correlation coefficient of 0.602, with a two-sided significance value of  $D =$   
153  $6.88 \times 10^{-20}$ , which equates to a 9- $\sigma$ -level detection. We also tested the effect on the calculated  
154 spectrum of including or excluding 100% relative humidity of ammonia (NH<sub>3</sub>), but found that this  
155 was completely undetectable due to ammonia's extremely low abundances at these temperatures.  
156 In case the ammonia abundance in Uranus' atmosphere is in reality highly supersaturated, we also  
157 tested the effect on the calculated spectrum of supersaturating NH<sub>3</sub> by factor of 1000, also shown  
158 in Fig. 4. However, we found that the absorption features of NH<sub>3</sub> do not coincide at all well with  
159 the difference spectrum, with correlation coefficients of only 0.271 (Pearson) and 0.256 (Spear-  
160 man), respectively. We thus conclude that NH<sub>3</sub> is not the source of the missing absorption. The  
161 correlation between the spectral discrepancy of the fit, when H<sub>2</sub>S is neglected, and the differences  
162 between the modelled spectra when H<sub>2</sub>S or NH<sub>3</sub> absorption is added are shown in Supplemental  
163 Fig. 2.

164 The retrieved relative humidity of the H<sub>2</sub>S profile needed to match the observed absorption  
165 features was  $113 \pm 12\%$ . Since the mole fraction of H<sub>2</sub>S decreases rapidly with height, this scaling  
166 factor is strongly weighted by the abundance of H<sub>2</sub>S just above the cloud tops, i.e. at 2–3 bar and

167 found to be 0.47 ppm, but is consistent with the H<sub>2</sub>S profile having 100% relative humidity in this  
168 region. However, this conclusion depends upon both the assumed temperature profile, which sets  
169 the saturated vapour pressure, and also the assumed methane profile, which affects the retrieved  
170 cloud-top pressure and thus the peak pressure level (and thus local temperature) of sensitivity  
171 to H<sub>2</sub>S. To test these effects we repeated our retrievals using a vertical profile of temperature  
172 and abundance estimated from Spitzer<sup>24</sup>, which has a lower CH<sub>4</sub> abundance of 3.2%, compared  
173 with 4% for the ‘F1’ profile<sup>3</sup>, but is slightly warmer at pressures greater than 1 bar, resulting in  
174 higher saturated vapour pressures of H<sub>2</sub>S. As might be expected, the lower CH<sub>4</sub> abundance of this  
175 profile led to the retrieved cloud opacity peaking at slightly higher pressures to achieve the required  
176 column abundance of CH<sub>4</sub> (Table 1) and the retrieved H<sub>2</sub>S relative humidity at the deeper cloud  
177 tops in the warmer atmosphere was only  $16 \pm 2\%$ . Since it is not clear which of these two profiles is  
178 more reliable, (although the ‘F1’ profile was found to be inconsistent with Spitzer observations<sup>24</sup>) it  
179 can be seen that although we clearly detect the presence of H<sub>2</sub>S at Uranus’ cloud tops, it is difficult  
180 to quantitatively determine its relative humidity. However, we can see from Table 1 that there is  
181 very good correspondence between the retrieved values of column abundance of H<sub>2</sub>S above the  
182 clouds for the two temperature profiles and also between the retrieved mole fraction of H<sub>2</sub>S at the  
183 cloud-top pressure level of  $(4.7 \pm 0.5) \times 10^{-7}$  for the ‘F1’ profile and  $(4.3 \pm 0.5) \times 10^{-7}$  for the  
184 Spitzer profile, where we have propagated the relative humidity retrieval errors.

185 Table 1 and Supplementary Figs. 3 – 11 show our fits at the other test points on Uranus’ disc,  
186 indicated in Fig. 1. At all locations except in Uranus’ northern polar ‘cap’ feature we found a clear  
187 improvement in our fit to the spectra when H<sub>2</sub>S absorption is included, indicating the presence of

188 H<sub>2</sub>S at the cloud tops (Table 1), with well defined column abundances of  $(2 - 5) \times 10^{19}$  molecule  
189 cm<sup>-2</sup> and cloud-top mole fractions of 0.4 – 0.8 ppm. All but one of the chosen points were on the  
190 central meridian, to keep the zenith angle as low as possible to minimise the computation time of  
191 our multiple scattering code, which uses more Fourier components in the azimuth decomposition  
192 direction as the zenith angle increases to maintain accuracy. However, point ‘2’ was chosen to be  
193 at roughly the same latitude as our reference area, but off the central meridian and closer to the  
194 limb to check that our retrieval was robust against zenith angle changes, which was found to be  
195 the case. The absence of a clear H<sub>2</sub>S signature near Uranus’ north pole seems to indicate lower  
196 H<sub>2</sub>S above the clouds in this region, in the same way that microwave observations found that the  
197 polar regions were depleted in microwave absorbers (H<sub>2</sub>S and NH<sub>3</sub>) at depth<sup>6</sup>. The abundance of  
198 methane above the clouds is also known to be reduced at these latitudes<sup>3,19</sup>. Alternatively, it could  
199 also be that the H<sub>2</sub>S signal is masked by increased abundance of tropospheric haze, but Table 1,  
200 which lists a haze ‘index’, given by the observed radiance in a methane absorbing band divided  
201 by the radiance at continuum wavelengths, does not suggest that the polar region is particularly  
202 affected by overlying haze. However, to explore this further requires a detailed examination of  
203 spectra in the polar regions, which is beyond the scope of this paper.

204         If we could be sure that the main observed cloud deck was vertically thin and composed of  
205 H<sub>2</sub>S ice, then we could constrain the abundance of H<sub>2</sub>S below it by equating the cloud base to  
206 the condensation level. However, the low retrieved single-scattering albedo of the cloud particles  
207 means that we cannot tell between whether we are seeing a vertically thin cloud based at 2–3 bar  
208 or just the top of a vertically extended cloud that extends to several bars. Instead, our detection of

209 H<sub>2</sub>S can be used to give a lower limit on its abundance below the observed cloud. Assuming the  
 210 main cloud is made of H<sub>2</sub>S ice, is vertically thin and is based at 3 bars, and that the STIS/Voyager-  
 211 2 ‘F1’ temperature profile<sup>3</sup> we have assumed is correct, the saturated mole fraction of H<sub>2</sub>S at the  
 212 3-bar level (where the temperature is 116.1K) is estimated to be  $1.1 \times 10^{-5}$ . Alternatively, using  
 213 the Spitzer profile<sup>24</sup>, the saturated vapour mole fraction at the 3-bar level (where the temperature  
 214 is 119.5 K) is  $2.5 \times 10^{-5}$ . Hence, we can conclude that the mole fraction of H<sub>2</sub>S at pressures  
 215  $> 3$  bar, immediately below the clouds must be  $> (1.0 - 2.5) \times 10^{-5}$ . We can compare this  
 216 with the expected abundances of H<sub>2</sub>S and NH<sub>3</sub> from microwave VLA studies<sup>5-7</sup>, who found the  
 217 abundance of H<sub>2</sub>S to be  $10 - 30 \times$  solar, and  $S/N > \sim 5$ , assuming solar abundances<sup>8</sup> of H<sub>2</sub>S/H<sub>2</sub>  
 218  $= 3.76 \times 10^{-5}$  and NH<sub>3</sub>/H<sub>2</sub> =  $1.74 \times 10^{-4}$  (giving N/S = 4.6). Using these values,  $10 \times$  solar H<sub>2</sub>S  
 219 and  $2 \times$  solar NH<sub>3</sub> would give a residual mole fraction of H<sub>2</sub>S above a deeper NH<sub>4</sub>SH cloud of at  
 220 least  $3 \times 10^{-5}$ , while for  $30 \times$  solar H<sub>2</sub>S and  $6 \times$  solar NH<sub>3</sub>, the expected residual H<sub>2</sub>S mole fraction  
 221 increases to  $9 \times 10^{-5}$ . Both these values are significantly greater than our estimated minimum  
 222 residual abundance, but are consistent with it and may suggest that the base of the cloud lies at  
 223 pressures greater than 3 bar. A more recent analysis of Spitzer Uranus observations<sup>24</sup> suggests a  
 224 residual H<sub>2</sub>S mole fraction of  $1.5 \times 10^{-5}$  in order to reconcile the millimetre spectrum with the  
 225 temperature profile derived from Spitzer, which is much closer to our estimate. Interpolating to  
 226 the pressure levels in our assumed ‘F1’ temperature-pressure profile<sup>3</sup> where the VLA and Spitzer  
 227 estimates of residual H<sub>2</sub>S abundance are equal to the saturated vapour pressure abundances we  
 228 deduce that the base of the main cloud must lie at a pressure of 3.1 – 4.1 bar. Alternatively, if  
 229 we assume the Spitzer temperature-pressure profile<sup>24</sup>, we find a pressure range 2.8 – 3.7 bar. The

230 fact that we detect H<sub>2</sub>S at all at Uranus' cloud tops confirms that the deep abundance of H<sub>2</sub>S must  
231 exceed that of NH<sub>3</sub> and hence that S/N > 4.6 × solar for the solar abundance ratios<sup>8</sup> assumed  
232 by the VLA study<sup>5,6</sup>. We note, however, that there are other, more recent estimates of the solar  
233 abundance ratios, for which the solar N/S value varies from 4.4<sup>25</sup> to 5.0<sup>26</sup>. Hence, to ensure that  
234 the deep abundance of H<sub>2</sub>S exceeds that of NH<sub>3</sub> we conclude that the S/N ratio in Uranus' bulk  
235 atmosphere exceeds 4.4–5.0 × solar. The clear detection of gaseous H<sub>2</sub>S above Uranus' clouds  
236 leads us to conclude that H<sub>2</sub>S ice likely forms a significant component of the main clouds at 1.2 – 3  
237 bar. To our knowledge the imaginary refractive index spectrum of H<sub>2</sub>S ice has not been measured  
238 and hence we cannot directly verify if our retrieved refractive index spectrum is consistent with  
239 H<sub>2</sub>S ice. However, very large imaginary refractive indices, such as we retrieve, are absent in  
240 the measured complex refractive index spectra of H<sub>2</sub>O, CH<sub>4</sub> and NH<sub>3</sub> ices. This suggests that  
241 if Uranus' main clouds are indeed formed primarily of H<sub>2</sub>S ice, the particles may not be pure  
242 condensates, but may be heavily coated or mixed with photochemical products drizzling down  
243 from the stratosphere above, lowering their single-scattering albedos.

## 244 1 References

- 246 1. de Kleer, K., Luszcz-Cook, S., de Pater, I., Ádámkóvics, M., Hammel, H.B., 2015 Clouds  
247 and aerosols on Uranus: Radiative transfer modeling of spatially-resolved near-infrared Keck  
248 spectra. *Icarus* 256, 120 – 137.
- 249 2. Irwin, P.G.J., de Bergh, C., Courtin, R., Bézard, B., Teanby, N.A., Davis, G.R., Fletcher,  
250 L.N., Orton, G.S., Calcutt, S.B., Tice, D., Hurley, J., 2012b. The application of new methane

- 251 line absorption data to Gemini-N/NIFS and KPNO/FTS observations of Uranus' near-infrared  
252 spectrum. *Icarus* 220, 369 – 382.
- 253 3. Sromovsky, L.A., Fry, P.M., Kim, J.H., 2011. Methane on Uranus: The case for a compact  
254 CH<sub>4</sub> cloud layer at low latitudes and a severe CH<sub>4</sub> depletion at high latitudes based on a  
255 re-analysis of Voyager occultation measurements and STIS spectroscopy. *Icarus* 215, 292 –  
256 312.
- 257 4. Weidenschilling, S.J., Lewis, J.S., 1973. Atmospheric and cloud structures of the Jovian plan-  
258 ets. *Icarus* 20, 465 – 76.
- 259 5. de Pater, I., Romani, P.N., Atreya, S.K., 1991. Possible microwave absorption by H<sub>2</sub>S gas in  
260 Uranus' and Neptune's atmospheres. *Icarus* 91, 220 – 233.
- 261 6. de Pater, I., Romani, P.N., Atreya, S.K., 1989. Uranus' deep atmosphere revealed. *Icarus* 82,  
262 288 – 313.
- 263 7. de Pater, I., Massie, S., 1985. Models of the millimeter-centimeter spectra of the giant planets.  
264 *Icarus* 62, 143 – 171.
- 265 8. Cameron, A.G.W., 1982. Elemental and Nuclidic Abundances in the Solar System. In *Essays*  
266 *in Nuclear Astrophysics* (C. A. Barnes, D. D. Clayton, and D. N. Schramm, Eds.), pp. 23-43,  
267 Cambridge Univ. Press, London/New York.
- 268 9. Niemann, H.B., et al., 1998. The composition of the jovian atmosphere as determined by the  
269 Galileo probe mass spectrometer. *J. Geophys. Res.* 103, 22831 – 22845.

- 270 10. Boissier, J., Bockelée-Morvan, Biver, N., Crovisier, J., Despois, D., Marsden, B.G., Moreno,  
271 R. 2007. Interferometric imaging of the sulfur-bearing molecules H<sub>2</sub>S, SO and CS in comet  
272 C/1995 O1 (Hale-Bopp). *Astron. Astrophys.* 475, 1131 – 1144.
- 273 11. Eberhardt, P., Meier, R., Krankowsky, D., Hodges, P.R., 1994. Methanol and hydrogen sulfide  
274 in comet P/Halley. *Astron. Astrophys.* 288, 315 – 329.
- 275 12. Noll, K.S., McGrath, M.A., Trafton, L.M., Atreya, S.K., Caldwell, J.J., Weaver, H.A., Yelle,  
276 R.V., Barnet, C., Edgington, S., 1995. HST Spectroscopic observations of Jupiter after the  
277 collision of Comet Shoemaker-Levy 9. *Science* 267, 1307 – 1313.
- 278 13. Lellouch, E., 1996. Chemistry induced by the impacts: Observations. IAU Colloquium 156;  
279 Proceedings of the Space Telescope Science Institute Workshop, held in Baltimore, Mary-  
280 land, May 9–12, 1995. Eds.: Keith S. Noll, Harold A. Weaver, Paul D. Feldman, Cambridge  
281 University Press, p. 213.
- 282 14. Irwin, P.G.J., Teanby, N.A., Davis, G.R., Fletcher, L.N., Orton, G.S., Tice, D., Kyffin, A.,  
283 2011. Uranus' cloud structure and seasonal variability from Gemini-North and UKIRT obser-  
284 vations. *Icarus* 212, 339 – 350.
- 285 15. Irwin, P.G.J., Teanby, N.A., Davis, G.R., Fletcher, L.N., Orton, G.S., Calcutt, S.B., Tice, D.,  
286 Hurley, J., 2012. Further seasonal changes in Uranus' cloud structure observed by Gemini-  
287 North and UKIRT. *Icarus* 218, 47 – 55.

- 288 16. Irwin, P.G.J., Teanby, N.A., de Kok, R., Fletcher, L.N., Howett, C.J.A., Tsang, C.C.C., Wil-  
289 son, C.F., Calcutt, S.B., Nixon, C.A., Parrish, P.D., 2008. The NEMESIS planetary atmo-  
290 sphere radiative transfer and retrieval tool. *J.Q.S.R.T.* 109, 1136 – 1150.
- 291 17. Campargue, A., Leshchishina, O., Wang, L., Mondelain, D., Kassi, S., 2013. The WKLMC  
292 empirical line lists (5852 – 7919  $\text{cm}^{-1}$ ) for methane between 80 K and 296 K: “Final” lists  
293 for atmospheric and planetary applications. *J. Molec. Spectrosc.* 291, 16 – 22.
- 294 18. Rothman, L.S., Gordon, I.E., Babikov, Y., Barbe, A., Benner, D.C., Bernath, P.F., et al, 2013.  
295 The HITRAN2012 molecular spectroscopic database, *J.Q.S.R.T.* 130, 4 – 50.
- 296 19. Karkoschka, E., Tomasko, M., 2009. The haze and methane distributions on Uranus from  
297 HST-STIS spectroscopy. *Icarus* 202, 287–309.
- 298 20. Fray, N., Schmitt, B., 2009. Sublimation of ices of astrophysical interest: A bibliographic  
299 review. *Plan. Space. Sci.* 57, 2053 – 2080.
- 300 21. Irwin, P.G.J., Tice, D.S., Fletcher, L.N., Barstow, J.K., Teanby, N.A., Orton, G.S., Davis,  
301 G.R., 2015. Reanalysis of Uranus’ cloud scattering properties from IRTF/SpeX observations  
302 using a self-consistent scattering cloud retrieval scheme. *Icarus* 250, 462 – 476.
- 303 22. Karkoschka, E., Tomasko, M., 2010. Methane absorption coefficients for the jovian planets  
304 from laboratory, Huygens, and HST data. *Icarus* 205, 674 – 694.
- 305 23. Sromovsky, L.A., Fry, P.M., 2007. Spatially resolved cloud structure on Uranus: Implications  
306 of near-IR adaptive optics imaging. *Icarus* 192, 527 – 557.



- 307 24. Orton, G.S., Fletcher, L.N., Moses, J.I., Mainzer, A., Hines, D., Hammel, H., Martin-Torres,  
308 J., Burgdorf, M., Merlet, C., Line, M.R., 2014. 1. Mid-Infrared spectroscopy of Uranus from  
309 the Spitzer Infrared Spectrometer: Determination of the mean temperature of the upper tropo-  
310 sphere and stratosphere. *Icarus* 243, 494 – 513.
- 311 25. Grevesse, N., Asplund, M., Sauval, A.D., 2007. The solar chemical composition. *Space Sci.*  
312 *Rev.* 130, 105 – 114.
- 313 26. Lodders, K., 2010. Solar System Abundances of the Elements, in *Principles and Perspectives*  
314 *in Cosmochemistry, Astrophysics and Space Science Proceedings*, ISBN 978-3-642-10351-3.  
315 Springer-Verlag Berlin Heidelberg, p. 379.

316 **Correspondence** Correspondence and requests for materials should be addressed to Patrick G. J. Irwin  
317 (email: [patrick.irwin@physics.ox.ac.uk](mailto:patrick.irwin@physics.ox.ac.uk)).

318 **Acknowledgements** We are grateful to the United Kingdom Science and Technology Facilities Council  
319 for funding this research and also to our support astronomers: Richard McDermid and Chad Trujillo (2009,  
320 2010). The Gemini Observatory is operated by the Association of Universities for Research in Astronomy,  
321 Inc., under a cooperative agreement with the NSF on behalf of the Gemini partnership: the National Science  
322 Foundation (United States), the Science and Technology Facilities Council (United Kingdom), the National  
323 Research Council (Canada), CONICYT (Chile), the Australian Research Council (Australia), Ministério da  
324 Ciência e Tecnologia (Brazil) and Ministerio de Ciencia, Tecnología e Innovación Productiva (Argentina).  
325 We thank Larry Sromovsky for providing the code used to generate our Rayleigh-scattering opacities. Glenn  
326 Orton was supported by NASA funding to the Jet Propulsion Laboratory, California Institute of Technology.

327 Leigh Fletcher was supported by a Royal Society Research Fellowship at the University of Leicester.

328 **Author Contributions** P.G.J.I. wrote the proposal to make the original observations and reduced the data  
329 and re-analysed it using the NEMESIS code; B.B. and R.G. assisted in identifying and validating the line  
330 data used. G.A.O. provided the Spitzer T-P profile used. L.N.F., N.A.T., D.T., and all co-authors contributed  
331 to the analysis, interpretation of the results, and all co-wrote the final paper.

332 **Competing Interests** The authors declare that they have no competing financial interests.

## 333 **2 Figure Legends**

334 Figure 1. Panel A: The appearance of Uranus at  $1.55 \mu\text{m}$ , observed with Gemini/NIFS on 2nd  
335 November 2010 at approximately 06:00UT, showing the position of the seven  $5 \times 5$  pixel test areas  
336 picked for retrieval analysis. Panel B: The appearance of Uranus at  $1.62 \mu\text{m}$ . Panel C: Reference  
337 spectrum of Uranus<sup>14</sup> analysed in this study, averaged over area ‘1’ just north of the equator, near  
338 the disc centre, with a mean latitude of  $15.3^\circ\text{N}$ , and error estimates shown in grey. Panel D: Mean  
339 strength listed in the k-distribution tables used in this study across the Gemini/NIFS spectral range.  
340 These absorption tables were generated from the WKL<sub>MC</sub>@80K+<sup>17</sup> database for  $\text{CH}_4$ , and from  
341 HITRAN2012<sup>18</sup> for  $\text{H}_2\text{S}$  and  $\text{NH}_3$ . These mean absorption coefficients have been computed at a  
342 temperature of 100 K and pressure of 1 atm, similar to conditions found at the tops of Uranus’ main  
343 visible clouds. Note that for  $\text{NH}_3$ , the linedata in HITRAN2012 terminate at  $1.587 \mu\text{m}$ , roughly  
344 half way through the  $\text{H}_2\text{S}$  absorption band.

345 Figure 2. Assumed pressure variation of temperature (left-hand panel) and condensible abun-

346 dance (right-hand panel) assumed in this study for Uranus. The temperature-pressure profile is  
347 based on the ‘F1’ profile<sup>3</sup>. The vertical variation of the CH<sub>4</sub> abundance is as described in the text.  
348 The abundances of NH<sub>3</sub> and H<sub>2</sub>S have simply been limited by their saturation vapour pressures.

349 Figure 3. Fits to average Gemini/NIFS observation of Uranus, made on 2nd November 2010  
350 at 15.3° N, using three different assumptions for the *a priori* imaginary refractive index spectrum,  
351 and excluding H<sub>2</sub>S and NH<sub>3</sub> absorption. The red line shows the results using  $n_i = 0.001 \pm 0.0005$ ,  
352 the black line shows the results using  $n_i = 0.01 \pm 0.005$ , while the blue lines show the results using  
353  $n_i = 0.1 \pm 0.05$ . Panel a) shows the fits to the measured spectra, panel b) shows the difference  
354 between the observed and modelled spectra. Panel c) shows the fitted imaginary refractive index  
355 spectra of the one type of particle assumed right hand plot, while panel d) shows the fitted cloud  
356 profiles (opacity/bar at 1.6  $\mu\text{m}$ ). In panels c) and d) the *a priori* value and range is marked in light  
357 grey, while the error range on the retrieved quantities is indicated in darker grey. The  $\chi^2/n$  of the  
358 fits is also shown in panel a).

359 Figure 4. Fits to the co-added Gemini/NIFS observation of Uranus in the wavelength range  
360 1.56 – 1.6  $\mu\text{m}$ . In the top plot, the observed reflectivity spectrum and estimated error is shown  
361 in grey. The fitted spectrum when H<sub>2</sub>S absorption is not included is shown in red, while the  
362 fitted spectrum when H<sub>2</sub>S absorption is included is shown in black. The bottom plot shows the  
363 differences between these fits and the observed spectrum using the same colours (i.e. red when  
364 H<sub>2</sub>S absorption is not included and black when it is), with the error range again shown in grey. The  
365 blue line in the bottom plot shows how the calculated spectrum for the fit when H<sub>2</sub>S absorption is

366 not included (i.e. red line in the top plot) changes when H<sub>2</sub>S absorption is added (leaving all other  
367 fitted parameters unchanged), assuming a profile with 100% relative humidity (RH). The cyan line  
368 shows how the calculated spectrum changes when NH<sub>3</sub> absorption is added, leaving all other fitted  
369 parameters unchanged, assuming a profile with 1000 times the *a priori* NH<sub>3</sub> profile with 100%  
370 RH.

## 371 **Methods**

372 **Spectral Data Sources** The main gaseous absorber in the H-band (1.4 – 1.8  $\mu\text{m}$ ) in Uranus' spec-  
373 trum is methane. The best available source of methane line data at low temperature in this range is  
374 the WKL<sub>MC@80K</sub>+<sup>17</sup> line database, which contains the positions, strengths, lower-state energies  
375 and empirical estimates of the rotational quantum number  $J$ , of lines measured at 80K and 296K.  
376 These lines are improved over the WK<sub>MC@80</sub><sup>27</sup> database, previously used to analyse the Gem-  
377 ini/NIFS observations reanalysed here for Uranus<sup>2</sup> as they include extra lines that were detected at  
378 296K, but not at 80K, and we have further improved our assignment of line widths, as described  
379 below. For the lines detected at 296K, but not 80K, lower state energies were defined so as to yield  
380 an intensity at 80 K just below the measurement sensitivity threshold. Hence, the contribution of  
381 these lines at cold temperatures bears significant uncertainty. For the lines detected at 80K, but not  
382 296 K, the lower state energies were arbitrarily set to  $-1.0 \text{ cm}^{-1}$ . These line data were converted  
383 to HITRAN format, using the listed strengths at 296 K directly for lines observed at both 80 K and  
384 296 K, and for lines observed only at 80K, we extrapolated their strengths to 296 K using the listed  
385 arbitrary lower state energy of  $-1.0 \text{ cm}^{-1}$  and total partition function (rotational + vibrational)

386 provided as part of HITRAN2012<sup>18</sup>. The spectral range covered by these data is 5852 – 7919  
387  $\text{cm}^{-1}$  (1.262 – 1.709  $\mu\text{m}$ ). These measurements were made for “natural” methane gas, for which  
388 the  $\text{CH}_3\text{D}/\text{CH}_4$  ratio is estimated<sup>17</sup> to be  $5 \times 10^{-4}$ . This is not suitable for calculations in Uranus’  
389 atmosphere, for which the most precise estimate<sup>28</sup> of  $\text{CH}_3\text{D}/\text{CH}_4$  is  $(2.96^{+0.71}_{-0.64}) \times 10^{-4}$  (using an  
390 isotopic enrichment factor<sup>29</sup> of  $f = 1.68 \pm 0.23$ ). Hence, lines for  $\text{CH}_3\text{D}$  were scaled in strength  
391 by 2.96/5. For the foreign-broadened line widths, we used  $J$ -dependent  $\text{H}_2$ - and He-broadened  
392 widths<sup>30</sup>, to which we fitted a 4th-order polynomial in  $J$ , using the widths calculated for  $J = 13$   
393 for higher values of  $J$  to prevent inaccurate extrapolation<sup>31,32</sup>. We assumed temperature depen-  
394 dence coefficients of these foreign-broadened widths for  $\text{H}_2$ -broadening<sup>33</sup> and He-broadening<sup>35</sup>.  
395 For the line shape, we used a Voigt function, but with sub-Lorentzian correction far from line cen-  
396 tre as recommended for  $\text{H}_2$ -broadening conditions<sup>36</sup>. However, we also tested the sub-Lorentzian  
397 corrections suggested for Titan spectra<sup>37</sup> and a sub-Lorentzian correction previously suggested for  
398 modelling Uranus spectra<sup>38</sup>. Using these three different line shapes we took account of all lines  
399 within  $250 \text{ cm}^{-1}$  of each calculation wavelength.

400 Spectroscopic line data for hydrogen sulphide ( $\text{H}_2\text{S}$ ) and ammonia ( $\text{NH}_3$ ) were taken from  
401 HITRAN2012<sup>18</sup>. The line widths and their temperature exponents were also taken from the foreign-  
402 broadened data listed in HITRAN2012. For  $\text{H}_2\text{S}$  these are  $\gamma_{air} = 0.074 \text{ cm}^{-1} \text{ atm}^{-1}$  and a tem-  
403 perature exponent of 0.75, for all lines. HITRAN2012 note that detailed laboratory investigations  
404 are needed to characterise how the line widths vary with the ro-vibrational quantum number, and  
405 there appears to be no published evidence on the appropriate values for an  $\text{H}_2/\text{He}$ -broadening  
406 atmosphere. Similarly, for  $\text{NH}_3$ , we used the published HITRAN2012 foreign-broadening param-

407 eters. If the absorption of  $\text{NH}_3$  had proved to be significant, we might have attempted to use line-  
408 broadening parameters more suited to  $\text{H}_2/\text{He}$ -broadening conditions. However, as reported in our  
409 paper, the absorption of  $\text{NH}_3$  was not detected in these observations and hence there was no error  
410 introduced by using the listed HITRAN2012 air-broadened widths. We also examined using Exo-  
411 MOL line data for  $\text{H}_2\text{S}$ <sup>39</sup> and found negligible differences in the spectra computed at Gemini/NIFS  
412 resolution with the HITRAN2012 line data. Since the HITRAN2012 line data are much easier to  
413 handle (they contain far fewer ‘hot lines’, which are only relevant for high-temperature calcula-  
414 tions) and probably have better constrained line frequencies, we decided to use HITRAN2012 for  
415 both  $\text{NH}_3$  and  $\text{H}_2\text{S}$  line data. In both cases, in the absence of any better information and in the  
416 expectation of weak absorptions (for which the exact line widths are less important), we used the  
417 published HITRAN2012 air-broadened widths and a Voigt line shape, with a line wing cut-off of  
418  $35 \text{ cm}^{-1}$  to account for typical sub-Lorentzian wing corrections.

419       The line data were converted to k-distribution look-up tables, or k-tables, covering the Gem-  
420 ini/NIFS H-band spectral range, with 20 g-ordinates, 15 pressures, equally spaced in log pressure  
421 between  $10^{-4}$  and 10 bar, and 14 temperatures, equally spaced between 50 and 180 K. These tables  
422 were precomputed with the modelled instrument line shape of the Gemini/NIFS observations, set  
423 to be Gaussian with a full-width-half-maximum (FWHM) of  $0.0003 \mu\text{m}$ , after an analysis of ARC  
424 lamp calibration spectra<sup>2</sup>.

425 **Observations and wavelength calibration** Observations of Uranus were made with Gemini-  
426 North’s Near-infrared Integral Field Spectrometer (NIFS) instrument in September 2009 and Octo-  
427 ber/November 2010<sup>14,15</sup>, with adaptive optics using Uranus’ nearby moons for wavefront sensing

428 (e.g. Ariel, Titania). NIFS’ H-band spectral resolution gives a Gaussian instrument function with  
429 spectral resolution of  $\text{FWHM} = 0.0003 \mu\text{m}$ . The wavelength calibration provided by the standard  
430 pipeline of Gemini/NIFS was found to be not quite accurate enough to match the spectral features  
431 observed here. The assumed wavelength of sample  $i$  in the spectrum is set to  $\lambda_i = \lambda_0 + (i - i_0)\lambda_1$   
432 , where  $i_0$  is the sample number of the ‘central’ wavelength, and the wavelength centre and step  
433 were initially assumed to be  $\lambda_0 = 1.55 \mu\text{m}$  and  $\lambda_1 = 0.000155 \mu\text{m}$ , respectively. By comparing  
434 the measured spectrum to our initial fitted spectrum we found that we could achieve a much better  
435 fit by modifying these values to  $\lambda_0 = 1.54995 \mu\text{m}$  and  $\lambda_1 = 0.00016036 \mu\text{m}$ . We used these values  
436 in the subsequent analysis.

437 **Uranus vertical profiles of temperature and gaseous abundance** The reference temperature  
438 and abundance profile used in this study (Fig. 2) is based on the ‘F1’ STIS/Voyager-2 profile<sup>3</sup>.  
439 This profile has a deep methane mole fraction of 4%<sup>19</sup>, and has a varying relative humidity with  
440 height above the condensation level. The He:H<sub>2</sub> ratio in this profile is set to 0.131 and the profile  
441 includes 0.04% mole fraction of Ne. To this profile we added abundance profiles of NH<sub>3</sub> and H<sub>2</sub>S,  
442 assuming arbitrary ‘deep’ mole fractions (i.e. above the putative NH<sub>4</sub>SH cloud) of 0.001 for both,  
443 and limited their abundance to not exceed the saturated vapour pressure in the troposphere as the  
444 temperature falls with height. As the abundances of these gases (and CH<sub>4</sub>) decrease with pressure  
445 the abundance of H<sub>2</sub> and He is adjusted to ensure the sum of mole fractions adds to unity (keeping  
446 He:H<sub>2</sub> = 0.131, or equivalently 12:88); the heights are calculated from the hydrostatic equation  
447 using the local temperature, gravitational acceleration and local mean total molecular weight.

448 For comparison we also performed retrievals using the temperature-pressure profile deter-

449 mined by from Spitzer observations of Uranus' mid-IR spectrum<sup>24</sup>, again with 'deep' NH<sub>3</sub> and  
450 H<sub>2</sub>S abundances of 0.001. H<sub>2</sub> and He were assumed to be present with a ratio 85:15, again ensur-  
451 ing the sum of mole fractions adds to unity at all heights.

452 **Radiative-transfer analysis** The vertical cloud structure was retrieved from the Gemini/NIFS ob-  
453 servations using the NEMESIS<sup>16</sup> radiative-transfer and retrieval code. NEMESIS models planetary  
454 spectra either using a line-by-line model, or by using the correlated-k approximation<sup>40</sup>. For speed,  
455 these retrievals were conducted using the method of correlated-k, but we regularly checked that  
456 we obtained the same model spectra (to within error) using a line-by-line approach. To model  
457 these reflected-sunlight spectra, a matrix-operator multiple-scattering model<sup>41</sup> was used, with 5  
458 zenith angles (upwards and downwards, respectively) and the number of required components in  
459 the Fourier azimuth decomposition determined from the maximum of the reflected or incident-  
460 solar zenith angles. The collision-induced absorption of H<sub>2</sub>-H<sub>2</sub> and H<sub>2</sub>-He was modelled with  
461 published coefficients<sup>42-44</sup>. Rayleigh scattering was also included for completeness, but was found  
462 to be negligible at these wavelengths.

463 To analyse the measured radiance spectra within our radiative transfer model we initially  
464 used the high-resolution 'CAVIAR' solar spectrum<sup>45</sup>, which we smoothed to the NIFS resolution of  
465  $\Delta\lambda = 0.0003\mu\text{m}$ . However, we found that this spectrum (and others, e.g.<sup>46,47</sup>) contained spurious  
466 'Fraunhofer lines' that did not seem to correspond to features seen at these wavelengths in the  
467 Uranus spectra. We must assume that the method used to generate these 'Extraterrestrial Solar  
468 Spectra' (ESS), namely measuring the solar spectrum at the ground at various zenith angles and  
469 extrapolating to an airmass of zero, leads to small errors at these wavelengths. Hence, we used



470 a smoothed version of the solar spectrum<sup>47</sup> in our calculations, omitting the spurious ‘Fraunhofer  
471 lines’, which we found matched our observations much more closely.

472 The observed spectrum (with  $n_y = 937$  spectral points) was fitted with NEMESIS using a  
473 continuous distribution of cloud particles whose opacity at 39 levels spaced between  $\sim 10$  and  
474  $\sim 0.01$  bar was retrieved. For this cloud profile the *a priori* opacity values (at  $1.6 \mu\text{m}$ ) were set to  
475  $0.001 \pm 0.0005 \text{ g}^{-1} \text{ cm}^2$  at all levels (equating to opacity/bar values of  $\sim 1$ ), with a ‘correlation  
476 length’ of 1.5 scale heights to ensure the profile was vertically smooth. NEMESIS treats cloud  
477 opacity as log values and so the error was converted to  $\pm 50\%$ . The particles were assumed to  
478 have a standard Gamma size distribution with mean radius  $1.0 \mu\text{m}$  and variance 0.05, which are  
479 typical values assumed in previous analyses. Using a previously published technique<sup>21</sup>, the imag-  
480 inary refractive index of these particles was set to 1.4 at a wavelength of  $1.6 \mu\text{m}$  and NEMESIS  
481 used to retrieve the imaginary refractive index spectrum. The *a priori* imaginary refractive index  
482 spectrum was sampled at every  $0.05 \mu\text{m}$  between  $1.4$  and  $1.8 \mu\text{m}$ , with a ‘correlation length’ of  
483  $0.1 \mu\text{m}$  set in the covariance matrix, to ensure that retrieved spectrum varied reasonably smoothly  
484 with wavelength. Hence there were  $n_x = 48$  free variables in our retrieval setup. At each iter-  
485 ation of the model, the real part of the particles’ refractive index spectrum was computed using  
486 the Kramers-Kronig relation<sup>48</sup>. Self-consistent scattering properties were then calculated using  
487 Mie theory, but the Mie-calculated phase functions were approximated with combined Henyey-  
488 Greenstein functions at each wavelength to smooth-over features peculiar to perfectly spherical  
489 scatterers such as the ‘rainbow’ and ‘glory’. This is justified since we expect the actual aerosols  
490 in the atmosphere of Uranus to be solid condensates, and thus non-spherical. However, assuming

491 these non-spherical particles are randomly orientated with respect to each other, the bulk scattering  
492 properties, such as cross-section and single-scattering albedo, are reasonably approximated with  
493 Mie theory<sup>34</sup>, especially if the phase functions are also modified as we describe.

494 Since methane is the main gaseous absorber we tested to see whether some of the approxi-  
495 mations assumed in the WKLMC@80K+<sup>17</sup> line database might be having an adverse effect on our  
496 calculations. We first checked whether excluding the lines observed at 296 K, but not at 80 K (and  
497 which are assigned a lower state energy high enough to reduce the computed strength at 80 K to  
498 be below the measurement noise limit) might significantly affect the calculated spectra, but found  
499 very little difference when these lines were neglected. We also checked the effect excluding the  
500 lines observed only at 80 K as well (and which are assigned an arbitrary lower state energy of 1  
501  $\text{cm}^{-1}$ ). In this case, the differences were larger, but on the whole the model correctly reproduced  
502 the shape and main features of the observed spectrum.

503 **Retrieval Tests** Supplementary Fig. 12 shows our fit to the Uranus spectrum, setting the *a pri-*  
504 *ori* imaginary refractive indices to  $0.01 \pm 0.005$  at all wavelengths and using the three different  
505 sub-Lorentzian line shapes for  $\text{CH}_4$  (neglecting  $\text{H}_2\text{S}$  and  $\text{NH}_3$  absorption). We found that each  
506 assumption for the sub-Lorentzian correction gave a very similar fit to the spectrum ( $\chi^2/n \sim$   
507 1.7–1.9), which was initially puzzling. However, the reason for this is easy to understand from  
508 Supplementary Fig. 12. The effect of different sub-Lorentzian corrections is most apparent on the  
509 shortwave side of the strong absorption band at  $1.7 - 1.8 \mu\text{m}$  and previous studies have tuned the  
510 correction to get the best match to the observed spectrum between 1.5 and  $1.62 \mu\text{m}$ . Our current  
511 model, however, can very easily fit this region by varying the imaginary refractive index spectrum

512 of the particles and it can be seen that very different imaginary refractive index spectra are retrieved  
513 for the three different sub-Lorentzian corrections, but very similar vertical cloud distributions and  
514 similar spectral fits. In other words, there is a degeneracy between the sub-Lorentzian corrections  
515 and the retrieved imaginary refractive index. In fact, we had to be careful not to allow the imagi-  
516 nary refractive index retrieval too much freedom. Early retrievals sampled the imaginary refractive  
517 index spectrum more finely ( $\Delta\lambda = 0.005\mu\text{m}$ ) over the  $1.56 - 1.6 \mu\text{m}$  range and significant part  
518 of the spectral variation of reflectivity was accounted for by variations in  $n_i$ , which it was difficult  
519 to justify as being realistic. We thus assumed the slow wavelength-to-wavelength variation in  $n_i$   
520 as described. Since the line shape recommended for H<sub>2</sub>-He atmospheres<sup>36</sup> gave a good fit to the  
521 observations, we chose to use this assumption in our final analysis.

522 **Scattering Properties** Since the fitted imaginary refractive index spectrum for our cloud particles  
523 has values of typically  $n_i \sim 0.06$ , this leads the particles to be quite absorbing. This can best be  
524 seen in Supplementary Fig. 1, where we compare the computed wavelength dependence of the  
525 extinction cross-section (normalised to  $1.6 \mu\text{m}$ ), the single-scattering albedo, and the asymmetry,  
526  $g$ , of the forward part of the fitted combined Henyey-Greenstein phase functions for the case when  
527 the *a priori* imaginary refractive indices were set to  $0.01 \pm 0.005$ . We found the back-scattering  
528 part of the phase-function to be insignificant. As we can see the single-scattering albedo has values  
529 of  $\varpi = 0.7 - 0.8$ , while the phase function asymmetry,  $g$ , is  $\sim 0.7$ .

### 530 **3 Data availability statement**

531 The data that support the plots within this paper and other findings of this study are available from  
532 the corresponding author upon reasonable request.

### 533 **4 Methods References**

534 27. Campargue, A., Wang, L., Mondelain, D., Kassi, S., Bézard, B., Lellouch, E., Coustenis, A.,  
535 de Bergh, C., Hirtzig, M., Drossart, P., 2012. An empirical line list for methane in the 1.26  
536 – 1.71  $\mu\text{m}$  region for planetary investigations ( $T = 80 - 300 \text{ K}$ ). Application to Titan. *Icarus*  
537 219, 110–128.  
538

539 28. Feuchtgruber, H., Lellouch, E., Orton, G., de Graauw, T., Vandenbussche, B., Swinyard, B.,  
540 Moreno, R., Jarchow, C., Billebaud, F., Cavalié, T., Sidher, S., Hartogh, P., 2013. The D/H  
541 ratio in the atmospheres of Uranus and Neptune from Herschel-PACS observations. *Astron.*  
542 *Astrophys.* 551, A126.

543 29. Lécluse, C., Robert, F., Gautier, D., Guiraud, M. 1996. Deuterium enrichment in giant planets.  
544 *Planet. Space Sci.* 44, 1579 – 1592.

545 30. Pine A. S., 1992. Self-,  $\text{N}_2$ -,  $\text{O}_2$ -,  $\text{H}_2$ -, Ar-, and He- broadening in the  $\nu_3$  band Q branch of  
546  $\text{CH}_4$ . *Journal of Chemical Physics* 97, 773 – 785.

547 31. Amundsen D. S., Baraffe I., Tremblin P., Manners J., Hayek W., Mayne N. J., Acreman D.  
548 M., 2014. Accuracy tests of radiation schemes used in hot Jupiter global circulation models,

549

Astron. Astrophys. 564, A59.

550

32. Garland, R., Irwin, P.G.J., 2017. Effectively calculating gaseous absorption in radiative transfer models of exoplanetary and brown dwarf atmospheres, Mon. Not. R. Astro. Soc.. (in preparation).

552

553

33. MargoIis J. S., 1993. Hydrogen broadening and collision-induced line shifts of methane at 4200  $\text{cm}^{-1}$ . J.Q.S.R.T. 49, 71 – 79.

554

555

34. Mishchenko M. I., Travis, L. D., Khan, R.A., West, R. A., 1997. Modeling phase functions for dustlike tropospheric aerosols using a shape mixture of randomly oriented polydisperse spheroids. J. Geophys. Res., 102, 16831 – 16847.

556

557

558

35. Varanasi P., Chudamani S., 1990. The temperature dependence of lineshifts, linewidths and line intensities of methane at low temperatures. J.Q.S.R.T. 43, 1 – 11.

559

560

36. Hartmann, J.-M., Boulet, C., Brodbeck, C., van Thanh, N., Fouchet, T., Drossart, P., 2002. A far wing lineshape for H<sub>2</sub> broadened CH<sub>4</sub> infrared transitions. J.Q.S.R.T. 72, 117 – 122.

561

562

37. de Bergh, C., Courtin, R., Bézard, B., Coustenis, A., Lellouch, E., Hirtzig, M., Rannou, P., Drossart, P., Campargue, A., Kassi, S., Wang, L., Boudon, V., Nikitin, A., Tyuterev, V., 2012. Applications of a new set of methane line parameters to the modeling of Titan's spectrum in the 1.58  $\mu\text{m}$  window. Planet. Space Sci. 61, 85 – 98.

563

564

565

566

38. L.A. Sromovsky, Fry, P.M., Boudon, V., Campargue, A., Nikitin, A., 2012. Comparison of line-by-line and band models of near-IR methane absorption applied to outer planet atmospheres. Icarus 218, 1 – 23.

567

568

- 569 39. Azzam, A. A. A., Tennyson, J., Yurchenko, S. N., Naumenko, O. V., 2016. ExoMol molecular  
570 line lists - XVI: The rotation-vibration spectrum of hot H<sub>2</sub>S. M.N.R.A.S. 460, 4063 – 4074.
- 571 40. Lacis, A.A., Oinas, V., 1991. A description of the correlated-k distribution method for mod-  
572 elling nongray gaseous absorption, thermal emission, and multiple scattering in vertically  
573 inhomogeneous atmospheres. J.Geophys.Res. 96, 9027 – 9063.
- 574 41. Plass, G.N., Kattawar, G.W., Catchings, F.E., 1973. Matrix operator method of radiative trans-  
575 fer. 1: Rayleigh scattering. Appl. Opt. 12, 314 – 329.
- 576 42. Borysow, A., 1991. Modeling of collision-induced infrared absorption spectra of H<sub>2</sub> – H<sub>2</sub>  
577 pairs in the fundamental band at temperatures from 20 to 300 K. Icarus 92, 273 – 279.
- 578 43. Borysow, A., 1992. New model of collision-induced infrared absorption spectra of H<sub>2</sub> – He  
579 pairs in the 2 – 2.5 μm range at temperatures from 20 to 300 K – An update. Icarus 96, 169 –  
580 175.
- 581 44. Zheng, C., Borysow, A., 1995. Modeling of collision-induced infrared absorption spectra of  
582 H<sub>2</sub> pairs in the first overtone band at temperatures from 20 to 500 K. Icarus 113, 84 – 90.
- 583 45. Menang, K.P., Coleman, M.D., Gardiner, T.D., Ptashnik, I.V., Shine, K.P., 2013. A high-  
584 resolution near-infrared extraterrestrial solar spectrum derived from ground-based Fourier  
585 transform spectrometer measurements. J.Geophys.Res. 118, 5319 – 5331.
- 586 46. Fiorenza, C., Formisano, V., 2005. A solar spectrum for PFS data analysis. Planet. Space Sci.  
587 53, 1009 – 1016.

- 588 47. Thuillier, G., Hersé, M., Labs, D., Foujols, T., Peetermans, W., Gillotay, D., Simon, P.C.,  
589 Mandel, H., 2003. The solar spectral irradiance from 200 to 2400 nm as measured by the  
590 SOLSPEC spectrometer from the ATLAS and EURECA missions, *Solar Physics* 214, 1 – 22.
- 591 48. Sheik-Bahae, M., 2005. Nonlinear Optics Basics. Kramers-Kronig Relations in Nonlinear  
592 Optics. In Robert D. Guenther. *Encyclopedia of Modern Optics*. Amsterdam: Academic Press.

Table 1: Retrieval results at all areas considered on Uranus' disc.

Area	Latitude	$p_1$	$f_{H_2S}$	$\chi^2/n$	$\chi^2/n_y$	$\Delta\chi^2$	$x_{H_2S}$	$A_{H_2S}$	$R_H$
1 <sup>a</sup>	15.3°N	1.99	113 ± 12	1.30	1.23	367.3	0.47	2.7	2.1
2	13.8°N	2.00	134 ± 19	1.04	0.99	140.7	0.58	3.3	2.3
3	15.3°S	2.10	123 ± 16	1.23	1.17	225.1	0.80	4.9	2.5
4	32.5°N	1.88	303 ± 45	1.31	1.24	218.7	0.82	4.4	2.6
5	44.7°N	1.66	474 ± 84	1.33	1.26	172.9	0.43	2.1	2.8
6 <sup>b</sup>	62.0°N	1.56	252 ± 211	1.31	1.24	1.8	0.13	0.6	3.9
7	4.9°N	1.98	96 ± 9	1.57	1.48	333.8	0.38	2.2	2.2
1 <sup>c</sup>	15.3°N	2.28	16 ± 2	1.36	1.29	292.1	0.43	2.9	2.1

Notes:  $p_1$  is the pressure(bar) where the cloud opacity to space is unity;  $f_{H_2S}$  is the retrieved H<sub>2</sub>S relative humidity (%);  $\chi^2/n$  is the reduced chi-squared statistic of the fit when H<sub>2</sub>S is included, where  $n = n_y - n_x = 889$ ;  $\chi^2/n_y$  is the chi-squared statistic of the fit when H<sub>2</sub>S is included, where  $n_y = 937$ ;  $x_{H_2S}$  is mole fraction of H<sub>2</sub>S (ppm) at  $p_1$ ;  $A_{H_2S}$  is the column amount of H<sub>2</sub>S ( $10^{19}$  molecule  $\text{cm}^{-2}$ ) above  $p_1$ ;  $R_H$  is a haze 'index' – the ratio of the average radiance from 1.63 – 1.64  $\mu\text{m}$  divided by the average radiance from 1.57 – 1.58  $\mu\text{m}$ , expressed as %.

Further notes: <sup>a</sup>Area 1 is the main area studied; <sup>b</sup>For polar area 6, where the radiance is lower, the measurement errors did not need to be multiplied by 1.6 ensure a good  $\chi^2/n$ ; <sup>c</sup>Same area as reference, but analysed using the Spitzer temperature profile, rather than 'F1'.



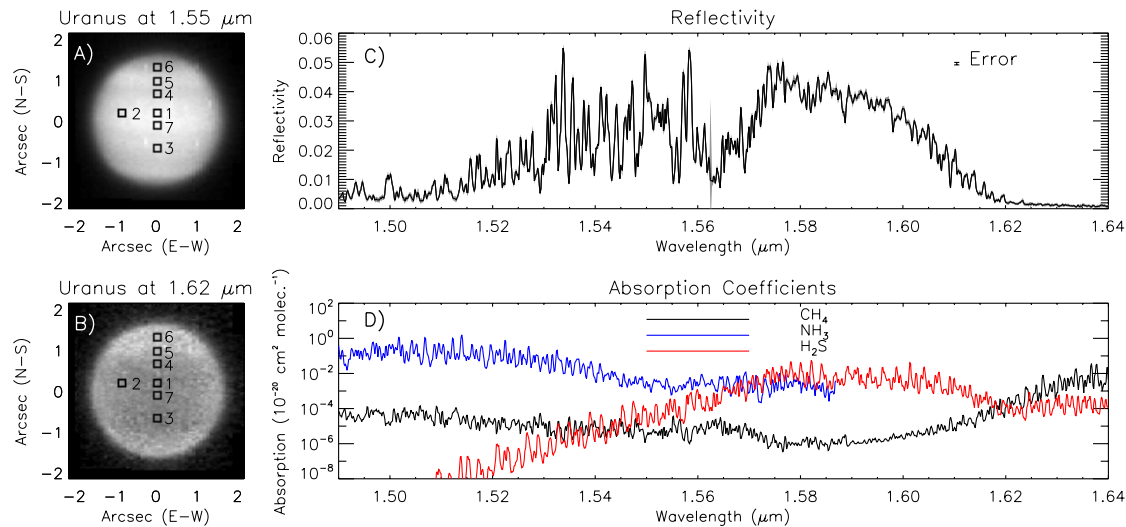


Figure 1: Panel A: The appearance of Uranus at 1.55  $\mu\text{m}$ , observed with Gemini/NIFS on 2nd November 2010 at approximately 06:00UT, showing the position of the seven  $5 \times 5$  pixel test areas picked for retrieval analysis. Panel B: The appearance of Uranus at 1.62  $\mu\text{m}$ . Panel C: Reference spectrum of Uranus<sup>14</sup> analysed in this study, averaged over area ‘1’ just north of the equator, near the disc centre, with a mean latitude of 15.3°N, and error estimates shown in grey. Panel D: Mean strength listed in the k-distribution tables used in this study across the Gemini/NIFS spectral range. These absorption tables were generated from the WKLMC@80K+<sup>17</sup> database for CH<sub>4</sub>, and from HITRAN2012<sup>18</sup> for H<sub>2</sub>S and NH<sub>3</sub>. These mean absorption coefficients have been computed at a temperature of 100 K and pressure of 1 atm, similar to conditions found at the tops of Uranus’ main visible clouds. Note that for NH<sub>3</sub>, the linedata in HITRAN2012 terminate at 1.587  $\mu\text{m}$ , roughly half way through the H<sub>2</sub>S absorption band.

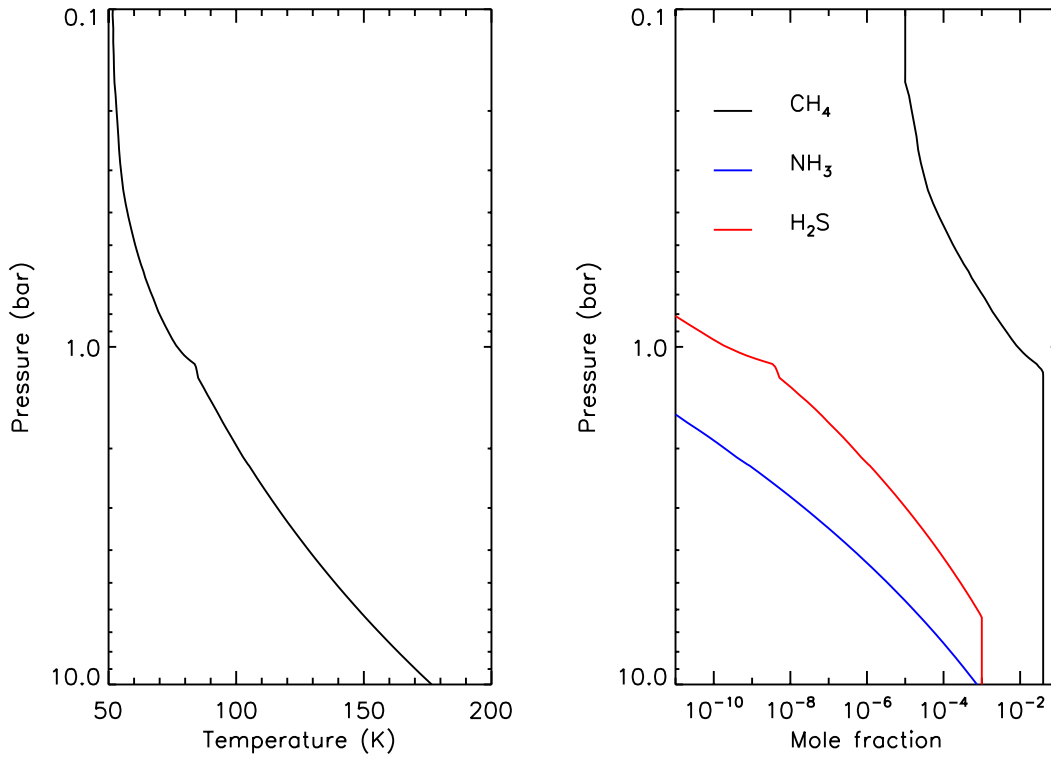


Figure 2: Assumed pressure variation of temperature (left-hand panel) and condensible abundance (right-hand panel) assumed in this study for Uranus. The temperature-pressure profile is based on the ‘F1’ profile<sup>3</sup>. The vertical variation of the CH<sub>4</sub> abundance is as described in the text. The abundances of NH<sub>3</sub> and H<sub>2</sub>S have simply been limited by their saturation vapour pressures.

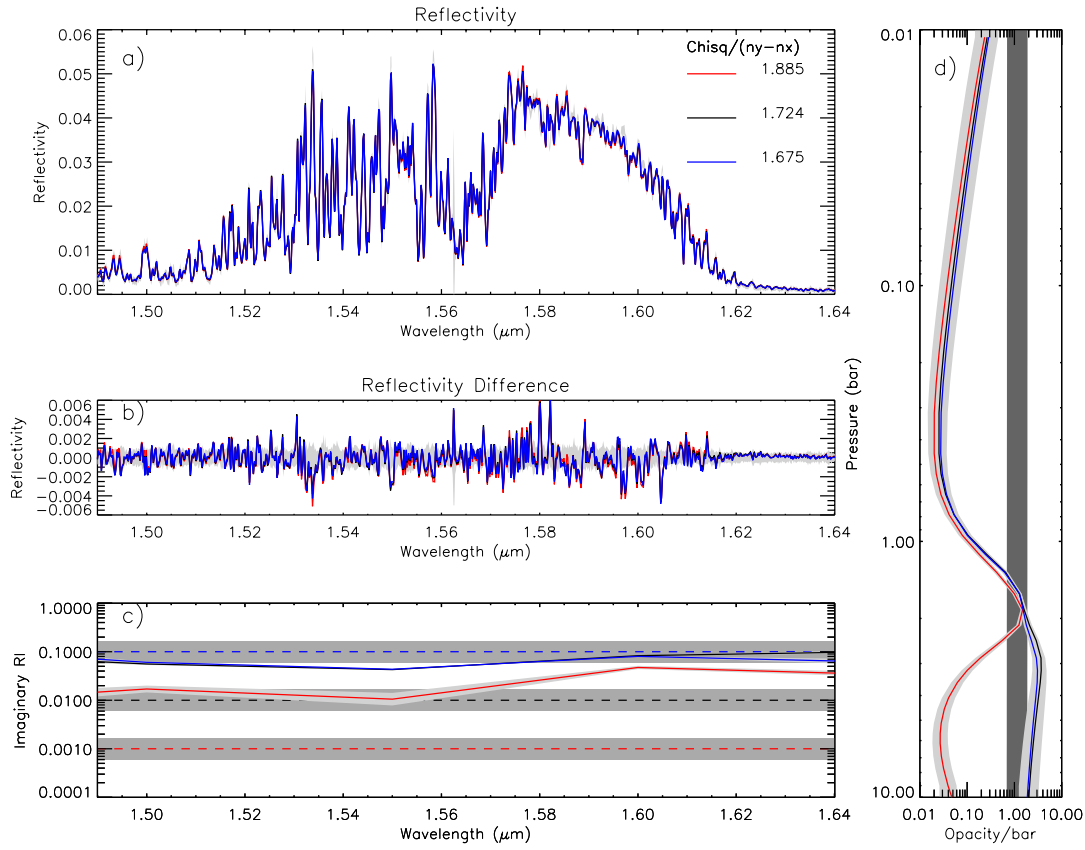


Figure 3: Fits to average Gemini/NIFS observation of Uranus, made on 2nd November 2010 at  $15.3^\circ$  N, using three different assumptions for the *a priori* imaginary refractive index spectrum, and excluding  $\text{H}_2\text{S}$  and  $\text{NH}_3$  absorption. The red line shows the results using  $n_i = 0.001 \pm 0.0005$ , the black line shows the results using  $n_i = 0.01 \pm 0.005$ , while the blue lines show the results using  $n_i = 0.1 \pm 0.05$ . Panel a) shows the fits to the measured spectra, panel b) shows the difference between the observed and modelled spectra. Panel c) shows the fitted imaginary refractive index spectra of the one type of particle assumed right hand plot, while panel d) shows the fitted cloud profiles (opacity/bar at  $1.6 \mu\text{m}$ ). In panels c) and d) the *a priori* value and range is marked in light grey, while the error range on the retrieved quantities is indicated in darker grey. The  $\chi^2/n$  of the fits is also shown in panel a).

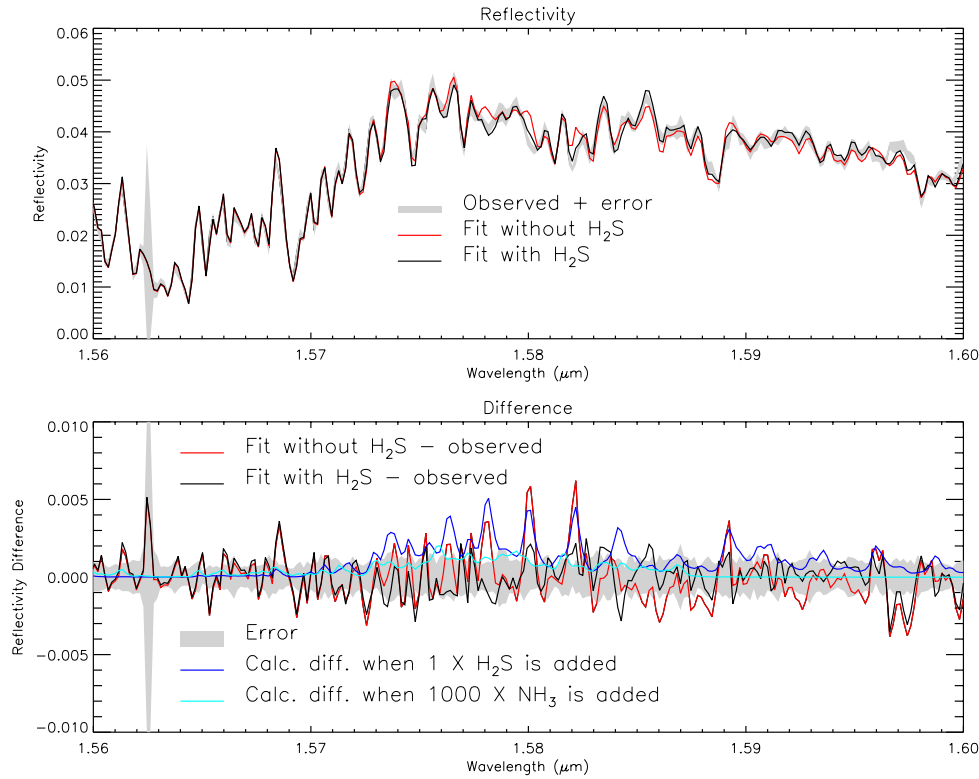


Figure 4: Fits to the co-added Gemini/NIFS observation of Uranus in the wavelength range 1.56 – 1.6  $\mu\text{m}$ . In the top plot, the observed reflectivity spectrum and estimated error is shown in grey. The fitted spectrum when  $\text{H}_2\text{S}$  absorption is not included is shown in red, while the fitted spectrum when  $\text{H}_2\text{S}$  absorption is included is shown in black. The bottom plot shows the differences between these fits and the observed spectrum using the same colours (i.e. red when  $\text{H}_2\text{S}$  absorption is not included and black when it is), with the error range again shown in grey. The blue line in the bottom plot shows how the calculated spectrum for the fit when  $\text{H}_2\text{S}$  absorption is not included (i.e. red line in the top plot) changes when  $\text{H}_2\text{S}$  absorption is added (leaving all other fitted parameters unchanged), assuming a profile with 100% relative humidity (RH). The cyan line shows how the calculated spectrum changes when  $\text{NH}_3$  absorption is added, leaving all other fitted parameters unchanged, assuming a profile with 1000 times the *a priori*  $\text{NH}_3$  profile with 100% RH.